A&A 512, A35 (2010)
DOI: 10.1051/0004-6361/200912947

Astronomy & Astrophysics

On the fundamental line of galactic and extragalactic globular clusters

M. Pasquato[1] and G. Bertin[2]

[1] Dipartimento di Fisica, Università di Pisa, Largo Bruno Pontecorvo 3, 56127 Pisa, Italy
e-mail: mario.pasquato@df.unipi.it
[2] Dipartimento di Fisica, Università degli Studi di Milano, via Celoria 16, 20133 Milano, Italy

Received 21 July 2009 / Accepted 2 November 2009

ABSTRACT

Context. In a previous paper, we found that globular clusters in our Galaxy lie close to a line in the ($\log R_e$, SB_e, $\log\sigma$) parameter space, with a moderate degree of scatter and remarkable axi-symmetry. This implies that a purely photometric scaling law exists, that can be obtained by projecting this line onto the ($\log R_e$, SB_e) plane. These photometric quantities are readily available for large samples of clusters, as opposed to stellar velocity dispersion data.
Aims. We study a sample of 129 Galactic and extragalactic clusters on this photometric plane in the V-band. We search for a linear relation between SB_e and $\log R_e$ and study how the scatter around the best-fit relation is influenced by both age and dynamical environment. We interpret our results in terms of testing the evolutionary versus primordial origin of the fundamental line.
Methods. We perform a detailed analysis of surface brightness profiles, which allows us to present a catalogue of structural properties without relying on a given dynamical model.
Results. We find a linear relation between SB_e and $\log R_e$, in the form $SB_e = (5.25 \pm 0.44)\log R_e + (15.58 \pm 0.28)$, where SB_e is measured in mag/arcsec^2 and R_e in parsec. Both young and old clusters follow the scaling law, which has a scatter of approximately 1 mag in SB_e. However, young clusters display more of a scatter and a clear trend in this with age, which old clusters do not. This trend becomes tighter if cluster age is measured in units of the cluster half-light relaxation time. Two-body relaxation therefore plays a major role, together with passive stellar population evolution, in shaping the relation between SB_e, $\log R_e$, and cluster age. We argue that the $\log R_e$-SB_e relation and hence the fundamental line scaling law does not have a primordial origin at cluster formation, but is rather the result of a combination of stellar evolution and collisional dynamical evolution.

Key words. globular clusters: general – Galaxy: structure

1. Introduction

In a previous paper (Pasquato & Bertin 2008, hereafter Paper I), we demonstrated that Galactic globular clusters (Galactic GCs) occupy a narrow region around a line in the ($\log R_e$, SB_e, $\log\sigma$) parameter space. This fundamental line is located within the fundamental plane of Galactic GCs (see Djorgovski 1995) and its existence was noted by Bellazzini (1998) based on principal component analysis techniques.

Bellazzini (1998) divided the observed Galactic GCs into two sets of inner GCs and outer GCs with respect to the Sun's orbit, and found that outer GCs have a dimensionality of 1 in the ($\log R_c$, SB_0, $\log\sigma$) space[1], while the dimensionality rises to 2 for inner GCs. He argued that inner GCs, which are closer to the Galactic bulge and interact more frequently with the disk, are more dynamically disturbed than outer GCs. Therefore, he suggested that dynamical interactions with the environment are more likely to disrupt than to preserve a fundamental line, which was then speculated to be primordial in origin.

By projecting the fundamental line onto the ($\log R_e$, SB_e) plane, in Paper I we predicted the existence of a purely photometric scaling law in the form of a linear relation between SB_e and $\log R_e$. This relation can be practically studied for a much larger sample than the fundamental plane, because velocity dispersion data is not required. In particular, bright clusters (both young and old) in the LMC, SMC, and Fornax galaxies may be included in the study, together with Galactic GCs. This allows a comparison to be made between the behaviors in the ($\log R_e$, SB_e) plane, of clusters that have significantly different ages and are associated with different environments.

The choice of using only photometric variables allows us to consider a relatively large sample of clusters with a substantial age spread. We are then able to attack the problem of the origin and evolution of the SB_e-$\log R_e$ scaling law by studying its dependence on cluster age and to look for evidence for or against the picture in which this scaling law originates primordially and diminishes with time because of dynamical evolution.

In the present paper, we follow Paper I in deriving cluster structural parameters in a model-independent way, in particular by avoiding fitting a given dynamical model to observational data. Some minor changes in the model-independent algorithm used are described in Sect. 2, where a detailed account of the data that we collect from the literature is also given. We compile a catalogue of fraction-of-light radii, average surface brightness, and absolute magnitudes, as a machine-readable table. Central cusps in the surface brightness profile have been observed in both old, Galactic GCs (Noyola & Gebhardt 2006) and

[1] The photometric quantities considered by Bellazzini (1998) are core/central quantities (i.e., core radius R_c and central surface brightness SB_0), as opposed to the half-light ones adopted in Paper I and in this paper (i.e., half-light radius R_e and average surface brightness within it SB_e).

extragalactic clusters (Noyola & Gebhardt 2007) and are predicted to form after core-collapse by N-body simulations (Trenti et al. 2010). Extended cluster envelopes have also been observed in young clusters in external galaxies (e.g., Larsen 2004; Schweizer 2004). The simple, single-mass, spherical isotropic King (1966) models that are usually taken to fit cluster surface brightness profiles have a flat core and sharp tidal cutoff and therefore have difficulties in modeling clusters with these features. The problem of extended envelopes prompted McLaughlin & van der Marel (2005) to refit a sample of Milky Way, LMC, SMC, and Fornax clusters with King models, power-law models, and Wilson (1975) models, finding that, for a sizeable fraction of the old GC population, King models do not perform more effectively than either Wilson (1975) or power-law models in fitting surface brightness profiles. More generally, the construction of physically-motivated self-consistent models continues to advance, by including features such as tidal flattening (e.g., see Bertin & Varri 2008), but model-independent approaches remain a valid complement to model-based analyses (see Kron & Mayall 1960). While a certain dependence on specific assumptions, such as the details of the extrapolation of the external part of surface brightness profiles, cannot be avoided, the catalogue of model-independent GC structural parameters presented in this paper naturally emerges as a tool useful for avoiding the potentially limiting assumptions required by dynamical models. The fundamental line and its scatter are presented in Sect. 3. Discussion and conclusions are given in Sect. 4.

2. The data

2.1. Distance moduli

We combined the distance moduli by Recio-Blanco et al. (2005) and Ferraro et al. (1999) for the Galactic GCs in our sample. Recio-Blanco et al. (2005) and Ferraro et al. (1999) list 72 and 61 objects respectively, with an overlap of 34, which provides a sample of 99 Galactic GCs with measured distance moduli. Both the apparent distance moduli in the $F555W$ band in Recio-Blanco et al. (2005) and the true distance moduli in Ferraro et al. (1999) are calibrated on the horizontal-branch standard candle. The distance moduli from Ferraro et al. (1999) are taken from Col. 8 of their Table 2, i.e., are based on the [M/H] metallicity scale. We converted the distance moduli by Recio-Blanco et al. (2005) to true distance moduli using the adopted $E(B-V)$ reddenings (see following subsection) and the relation between reddening and extinction in the $F555W$ band from Table 12 of Holtzman et al. (1995). For the data in the overlap of the Ferraro et al. (1999) and Recio-Blanco et al. (2005) samples, we took the error-weighted average value of the true distance modulus. In Paper I, we adopted quite conservative uncertainties in distance moduli, with a rescaling in the error bars to include systematic errors and an estimate of the error caused by the limited knowledge of the amount of α-enhancement. This procedure allowed us to prove that the scatter about the fundamental plane is not caused by observational errors alone, even though conservatively estimated. For the purpose of compiling the catalogue described in Sect. 2.8, we consider the errorbars quoted by the authors of the respective measurements and combine them in the standard way. For the extragalactic GCs in our sample, we adopt the distance to the host galaxy as the cluster's distance, following McLaughlin & van der Marel (2005), with the exception of the two clusters NGC 1466 and NGC 1841 which, while being listed as part of the LMC GC system by McLaughlin & van der Marel (2005), have an independent distance modulus measurement by Recio-Blanco et al. (2005). The extragalactic sample of McLaughlin & van der Marel (2005) comprises 68 GCs. Thus, the sample of both Galactic and extragalactic GCs with measured distance moduli comprises 165 objects.

2.2. Reddening

For Galactic GCs, we combined reddening data by Ferraro et al. (1999) and Recio-Blanco et al. (2005). For reddenings present in both listings, we adopted the error-weighted average. Errors are assumed to be 10% of the adopted reddening value, as in Paper I. The clusters NGC 6304, NGC 6316, NGC 6342, NGC 6356, NGC 6388, NGC 6441, NGC 6539, NGC 6624, and NGC 6760 have their distance modulus measured by Recio-Blanco et al. (2005), but reddening was listed for them by neither Recio-Blanco et al. (2005) nor Ferraro et al. (1999). Therefore, for these clusters, we chose to use the reddening values provided by Harris (1996).

2.3. Surface brightness profiles: apparent magnitudes and effective radii

The model-independent procedure based on spline-smoothing that we used for extracting integrated apparent magnitudes and fraction-of-light radii from the surface brightness profiles of GCs does not differ substantially from the one described in Paper I. Three differences are worth mentioning:

- The smoothing parameter of the spline-fitting algorithm is now adjusted interactively by directly examining how much the resulting spline matches the GC surface brightness data.
- The extrapolation that is taken past the outermost observed point in the surface brightness profile assumes the projected luminosity density decreases as a power law with projected distance from the GC center. A discussion of this power-law behavior of the outer part of the GC surface brightness profiles is given in Sect. 3. The power law is truncated at $5 \times r_{\rm ou}$, where $r_{\rm ou}$ is the outermost observed radius. The contribution to the integrated luminosity from the extrapolated profile is usually not influenced significantly by changes in this cutoff. The power-law exponent is determined by fitting the outer points in the surface brightness profile. The exact number of points used for each cluster is again defined interactively. GCs with a contribution to the integrated apparent magnitude from the extrapolated profile that exceeds 0.5 mag are removed from the sample.
- Automated outlier rejection based on comparison with literature data does not take place. Instead, the cluster surface brightness profiles are inspected visually, and as a result those of NGC 2419, NGC 4372, NGC 6101, NGC 6541, and NGC 6535 are excluded from the sample due to their poor quality.

A sample of 125 surface brightness profiles was acquired from Trager et al. (1995) for Galactic GCs, and 68 surface brightness profiles of extragalactic clusters were taken from McLaughlin & van der Marel (2005). We have a combined sample of 145 GCs with model-independent structural parameters, after removing the clusters with an excessive (as defined above) contribution to the apparent luminosity from the extrapolated profile and the five listed explicitly.

2.4. Shape of the surface brightness profile at the GC center

In Paper I, we found an unexpected correlation between residuals to the fundamental plane of Galactic GCs and the central logarithmic slope of the GC surface brightness profile defined and measured by Noyola & Gebhardt (2006). In the present paper, the slopes measured by Noyola & Gebhardt (2007) for extragalactic clusters are combined with those measured by Noyola & Gebhardt (2006), producing a sample of 68 GCs with measured slopes.

2.5. Extrapolation of the surface brightness profile

Most GC surface brightness profiles can be accurately fitted in their outer parts with a power-law luminosity density I per unit area given by

$$I \propto R^{-a} \tag{1}$$

We determine the value of the exponent a for the sample of 145 GCs with quality surface brightness profiles for which we compute the model-independent structural parameters. This best-fit relation is then used to extrapolate the surface brightness profile and calculate the cluster integrated apparent magnitude.

2.6. Distance from the center of the host galaxy and orbital parameters

To assess the role of environment-driven dynamical evolution in establishing or eliminating the SB_e-$\log R_e$ relation, we use distances from the center of the host galaxy listed by McLaughlin & van der Marel (2005) as a quantitative measure of the interaction. This approach is similar to that of Bellazzini (1998), who divided Galactic GCs on the basis of Galactocentric distance to study the fundamental line of GCs.

In principle, the size of the Roche lobe is a more accurate estimator of the amount of tidal disturbance that the host galaxy exerts on a cluster. A cluster of mass M_{GC} in a circular orbit with an angular velocity Ω at distance R_G from the center of its host galaxy (taken to be spherically symmetric) has a tidal radius (see Bertin & Varri 2008)

$$r_T = \left(\frac{GM_{GC}}{\Omega^2 \nu}\right)^{1/3}, \tag{2}$$

where $\nu \equiv 4 - \kappa^2/\Omega^2$ is a coefficient that depends on the rotation curve $V = \Omega R$ associated with the galaxy. For a flat rotation curve, $\nu = 2$ and

$$r_T \propto R_G^{2/3} M_{GC}^{1/3}, \tag{3}$$

where the constant of proportionality varies from one galaxy to another. The sample of clusters with model-independent structural parameters, host-galaxy distances, and masses estimated by McLaughlin & van der Marel (2005) consists of 114 GCs. We use Eq. (3) to calculate the tidal radius for 61 clusters in the Milky Way and 40 in the LMC; we do not consider either the SMC or Fornax objects because their sample size would be too small. Of course, a thorough analysis would require a discussion of how the available projected data truly constrain the relevant intrinsic quantities which appear in Eqs. (2) and (3) (see also Spitzer 1987; Heggie & Hut 2003) but this is beyond the scope of the present paper. McLaughlin & van der Marel (2005) list only sky-projected distances for LMC, SMC, and Fornax clusters. Full three-dimensional distances are available only for Galactic GCs.

Measuring the strength of the dynamical interaction with the host galaxy using detailed orbital data instead of instantaneous distances would be more accurate, but these data are available only for a much smaller subset of Galactic GCs. Allen et al. (2006) calculate the orbits of 48 GCs in a model Milky Way potential, yielding average pericenter distances and orbital eccentricities. The sample of clusters with such an orbit determination and model-independent structural parameters consists of 36 GCs. Allen et al. (2006) calculate orbits based on GC radial velocity and proper motion data, based on either an axisymmetric or a barred model Galactic potential. In the following, we use orbital data from the axisymmetric model, but we checked that our results do not differ significantly if the barred model is assumed instead.

2.7. Ages and timescales

Marín-Franch et al. (2009) obtain GC relative ages from HST/ACS data acquired by the ACS Survey of Galactic globular clusters, while De Angeli et al. (2005) list ages from either ground-based photometry or HST snapshot data. For both samples, we adopt the ages based on the Carretta & Gratton (1997) metallicity scale, normalize both sets of relative ages to NGC 104, and adopt the average value for the combined samples. NGC 6287 is the oldest cluster in the combined sample, so we set its age to be 13 Gyr to determine the absolute ages of the combined set of Galactic GCs. The young clusters of the LMC, SMC, and Fornax are assigned ages following McLaughlin & van der Marel (2005). The final sample of Galactic and extragalactic GCs with measured ages contains 131 objects.

Relaxation times at the half-light radius are taken from McLaughlin & van der Marel (2005). Since McLaughlin & van der Marel (2005) analyze the GC surface brightness profiles in a model-dependent way, we adopt the values based on King (1966) model fits. The processes driven by two-body interactions, such as mass loss by means of the evaporation of stars, mass segregation of stars of different masses within the GC, and core collapse, are expected to occur over a timescale of several relaxation times. The ratio of age to relaxation time is thus a measure of the "dynamical age", i.e., the degree of relaxation of a given cluster.

Allen et al. (2006) use the orbits that they calculate for their sample of 48 GCs to compute destruction rates for bulge- and disk-shocking[2]. These are the reciprocals of the natural timescales against which cluster age is compared to quantify the amount of dynamical interaction with the host Galactic environment a that given GC has suffered.

In the following, we denote cluster ages by τ_a, half-light relaxation times by τ_r, disk-shocking destruction rates by $1/\tau_d$, and bulge-shocking destruction rates by $1/\tau_b$.

2.8. The catalogue

For the adopted sample of 129 GCs, Table 1 lists the integrated apparent V-band magnitude obtained by using our model-independent profile smoothing method, the adopted reddening and true distance modulus, the log projected half-light radius (in arcsecs), and the value of the exponent a obtained by fitting a power-law to the outermost part of the GC surface brightness profile (see Eq. (1)). Table 2 lists the average V-band

[2] The Allen et al. (2006) destruction rates differ significantly from other literature values (e.g., see Kruijssen & Mieske 2009). This should be kept in mind when considering our results in Sect. 3.6.

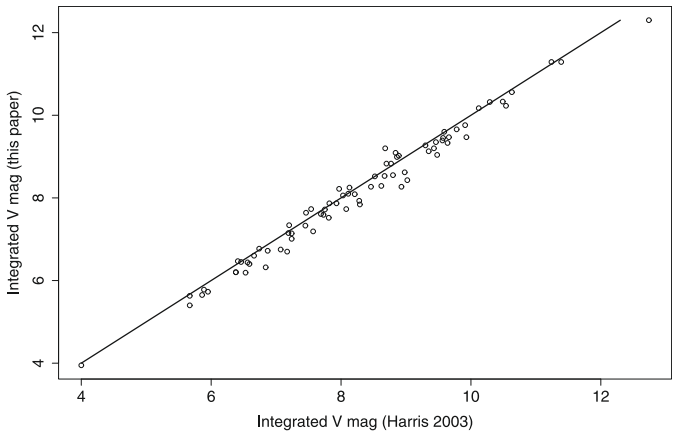

Fig. 1. Comparison between the integrated apparent V-band magnitudes of GCs derived in the present paper with the values listed by Harris (1996). The superimposed line represents the identity. The magnitudes we derive are systematically fainter by approximately 0.12 mag in the median with respect to the Harris (1996) values.

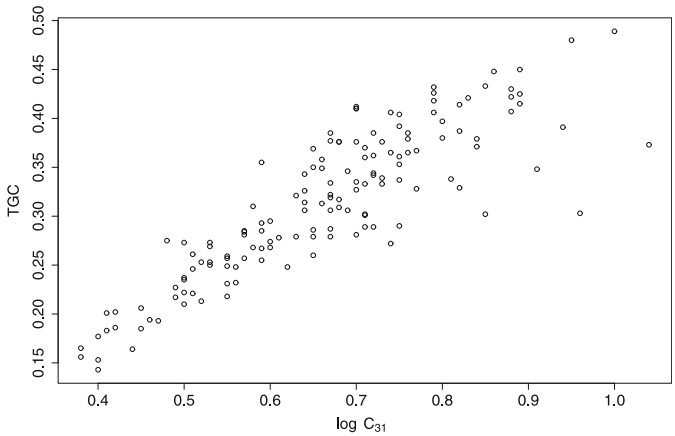

Fig. 2. Relation between the C_{31} and the TGC non-parametric concentration indices for the adopted sample of 145 GCs with quality surface brightness profiles.

surface brightness within the half-light radius SB_e (in mag/arcsec^2), half-light radius $\log R_e$ (in parsecs), absolute magnitude M_V, and residuals in SB_e to the fitted SB_e-$\log R_e$ linear relation.

To assess the impact of model-dependence on the GC structural parameters, we compare the luminosities that we obtained here with the values listed in the catalogue by Harris (1996) for Galactic GCs. The sample with parameters available both in the Harris catalogue and in this paper contains 76 GCs. Figure 1 compares our V-band integrated apparent magnitudes with the Harris (1996) values. The magnitudes derived in the present paper are fainter than those of Harris (1996) by 0.12 mag in the median. The rms scatter of the differences is 0.2 mag. Nine clusters exhibit a discrepancy of 0.4 mag or more between the integrated apparent magnitude that we derive here and the Harris (1996) value. These clusters are Arp 2, NGC 4590, NGC 5466, NGC 5634, NGC 6218, NGC 6316, NGC 6366, NGC 6584, and NGC 6809. With the exception of NGC 6584 and NGC 6316, a visual inspection of the Trager et al. (1995) surface brightness profiles of these clusters detects either a very noisy profile or puzzling features such as a non-monotonic behavior.

2.9. Fraction of light radii and non-parametric concentration measurements

Fraction of light radii for fractions other than 1/2 are also obtained for each GC and listed in Table 3, thus providing an update and extension of the study by Trager et al. (1995), who list the fraction of light radii (from 10% to the half-light radius) for their sample of Galactic GCs. We recall that the ratio of two different fraction of light radii defines dimensionless shape parameters for the surface brightness profile, which for King-model clusters should be on a one-to-one relation with the concentration parameter c. McLaughlin & van der Marel (2005) call for "a more generally applicable concentration index able to represent the spatial extent or potential depth of any cluster in a more model-independent way (so as to allow, e.g., for a combined analysis of clusters that may not all be described well by the same type of model)".

Using our fraction of light radii, we obtain the coefficients $C_{21} = r_e/r_{25\%}$, $C_{32} = r_{75\%}/r_e$, and $C_{31} = r_{75\%}/r_{25\%}$. These concentration indicators do not rely on model-based assumptions on the shape of the surface brightness profile, and can easily be calculated for a given model surface brightness profile. We also obtain the so-called Third Galaxy Concentration (TGC) index introduced by Graham et al. (2001) to improve the stability of non-parametric indicators of galaxy concentration as a function of the radial extension of the observed luminosity profile. The TGC coefficient is defined to be the ratio of the light contained within $r_e/3$ to the light contained within the half-light radius r_e[3]. To the best of our knowledge, this is the first calculation of these indices for GCs, while the use of non-parametric concentration indicators for galaxies dates to the studies of Fraser (1972) and de Vaucouleurs (1977).

Figure 2 shows the TGC index as a function of $\log C_{31}$ for the adopted sample of 145 GCs with quality surface brightness profiles. We find a strong correlation with $r = 0.87$. This is an indirect check that GC surface brightness profiles are described well by a one-parameter family of models. The observed linear correlation still leaves room for ingredients such as mass segregation or IMBHs to introduce deviations from this simple one-parameter picture.

3. Results

3.1. The SB_e-log R_e relation

As anticipated, based on the projected fundamental line argument of Paper I, we do find a linear relation between V-band SB_e and $\log R_e$ for the adopted sample of 129 GCs, of the form

$$SB_e = (5.25 \pm 0.44) \log R_e + (15.58 \pm 0.28), \quad (4)$$

where the coefficients are obtained by biweight (e.g., see Mosteller & Tukey 1977) fitting SB_e as a function of $\log R_e$, and errors are derived by bootstrap resampling. The scatter about the relation is 1.04 mag in SB_e, as quantified by the standard deviation of its residuals. Figure 3 shows the results for our catalogue of 129 GCs in the ($\log R_e$, SB_e) plane, different symbols representing the various host galaxies.

Equation (4) results from neglecting the errors in the individual data-points, an approach which is usually taken in the

[3] This is the choice that we adopt in the present paper, but in principle fractions other than 1/3 could be chosen, leading to slightly different definitions of TGC.

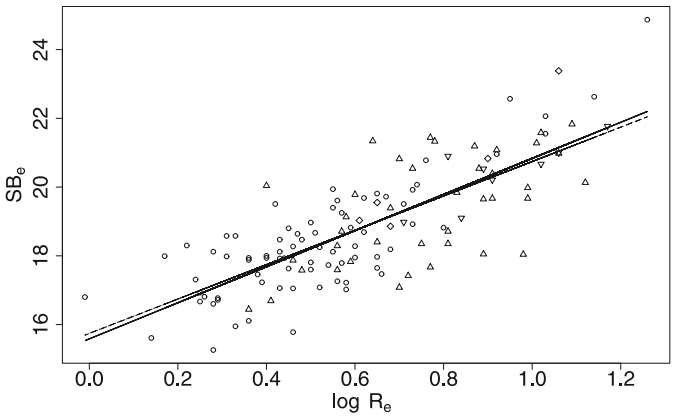

Fig. 3. Relation between V-band SB_e and $\log R_e$ for our catalogue of 129 GCs. Open circles are Galactic GCs, upwards facing triangles are LMC clusters, downwards facing triangles are SMC clusters, and diamonds are Fornax clusters. The solid line is the linear biweight fit of SB_e versus $\log R_e$ over the entire sample (see Eq. (4)). The thinner dashed line corresponds to a slope of exactly 5 (see Eq. (6)).

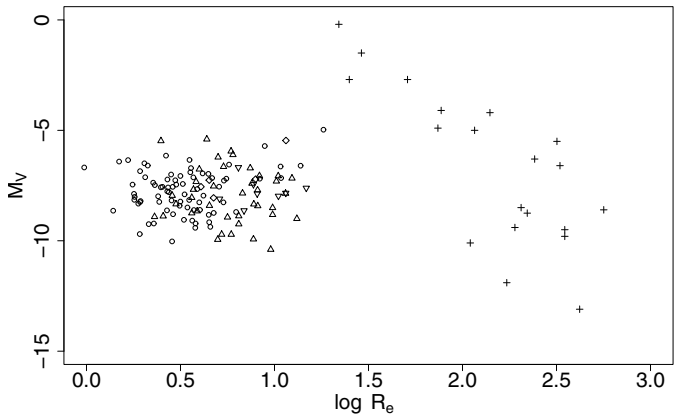

Fig. 4. Absolute integrated V-band magnitude M_V as a function of $\log R_e$ (in parsec) for our sample of 129 GCs (open circles are Galactic GCs, upwards facing triangles are LMC clusters, downwards facing triangles are SMC clusters, and diamonds are Fornax clusters) and the sample of 21 nearby dwarf spheroidal galaxies by van den Bergh (2008) (crosses).

literature (e.g., Djorgovski 1995). If, on the other hand, these errors are included in an ordinary least-squares regression fit, we obtain

$$SB_e = (6.09 \pm 0.40) \log R_e + (15.11 \pm 0.25). \quad (5)$$

The slopes of Eqs. (4) and (5) are consistent with each other within 3-σ.

3.2. Interpretation

Equation (4) is compatible to within 1 σ with

$$SB_e = 5 \log R_e + k, \quad (6)$$

which, for a given k, describes the locus of constant absolute magnitude $M_V = SB_e - 5 \log R_e$ within the $(\log R_e, SB_e)$ plane. Therefore, the clusters of our sample show no systematic trend of absolute magnitude with half-light radius, even though the spanned magnitude range is large.

This behavior is evident from Fig. 4, where we plot V-band integrated absolute magnitude M_V as a function of $\log R_e$ for GCs (identified by parent galaxy symbols as in Fig. 3) and for nearby dwarf spheroidal galaxies (the data for the latter are taken from van den Bergh 2008). While dwarf spheroidals show a clear trend of absolute magnitude with half-light radius, GCs form an almost perfect scatter plot, independent of their parent galaxy.

Quantitatively, by fitting a linear relation to M_V as a function of $\log R_e$ for the full sample of 129 GCs, we obtain

$$M_V = (0.3 \pm 0.4) \log R_e - (8.0 \pm 0.2) \quad (7)$$

where the $\log R_e$ coefficient does not differ significantly from 0.

Therefore, the existence of a linear SB_e-$\log R_e$ relation appears to reflect the statement that GCs have a luminosity independent of size. For a constant mass-to-light ratio M/L, this requirement dictates that GCs have a mass distribution that does not depend on their physical size. For Galactic GCs, this is a well-known fact (e.g., see Djorgovski & Meylan 1994), which has also been recently confirmed for extragalactic clusters (see Barmby et al. 2007) and is at the basis of the explanation proposed by Bellazzini (1998) for the existence of a fundamental line.

Even if Galactic, LMC, SMC, and Fornax clusters are considered separately, no significant trend of M_V with $\log R_e$ emerges, i.e., the independence of total luminosity on cluster size is apparently universal.

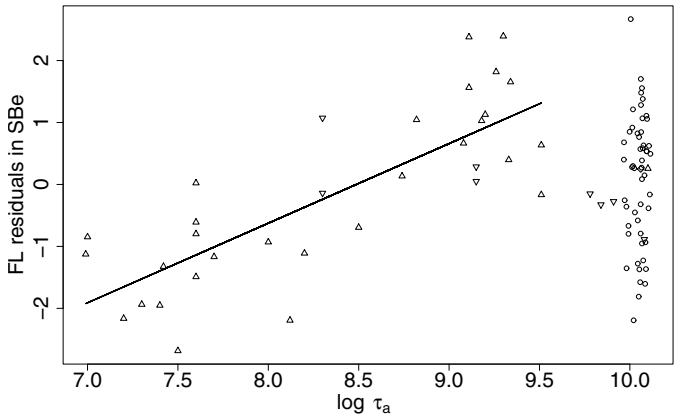

Fig. 5. Trend of residuals to the SB_e-$\log R_e$ relation with cluster age. Open circles are Galactic GCs, upwards facing triangles are LMC clusters, downwards facing triangles are SMC clusters, and diamonds are Fornax clusters. The solid line is the linear least squares fit of residuals versus log age for clusters younger than 4 Gyr. The old GCs are not located along the extrapolation of the correlation line for the younger clusters, which indicates that the young, massive clusters that are in the SMC, LMC, and Fornax now, are not likely to be similar to the YMCs that were the progenitors of the old GCs (see text for a discussion).

3.3. A trend of residuals with age for young clusters

The residuals to the fitted SB_e-$\log R_e$ relation are plotted against cluster age in Fig. 5. The residuals are defined as the difference between the true surface brightness and that predicted by the fitted linear relationship, so that a positive residual means a fainter surface brightness. Based on the assumption of a constant mass-to-light ratio, this implies a lower surface density. The plot shows a rather different behavior for young and old clusters. Old clusters, which we define to have age in excess of 4 Gyr, are mainly Galactic GCs and their residuals show no significant trend with age (the correlation coefficient is $r = 0.08$, compatible with 0 according to a t-test). The residuals of clusters younger than 4 Gyr, instead show a clear trend with age, with $r = 0.79$ and a highly significant t-test p-value of 5.4×10^{-8}. Moreover, Fig. 6 shows that these young clusters exhibit a larger scatter about the fitted line, as quantitatively confirmed by the standard deviation of their residuals with respect to it, which is 1.37 mag in SB_e as

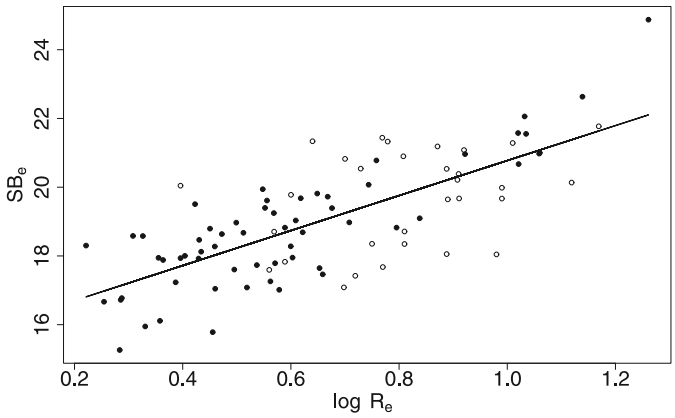

Fig. 6. Relation between V-band SB_e and $\log R_e$ for the 91 GCs in our sample with a reliable age determination. The solid line is the biweight linear fit to this restricted sample, with a slope of 5.09. Open circles are clusters younger than 4 Gyr, solid circles are GCs older than 4 Gyr.

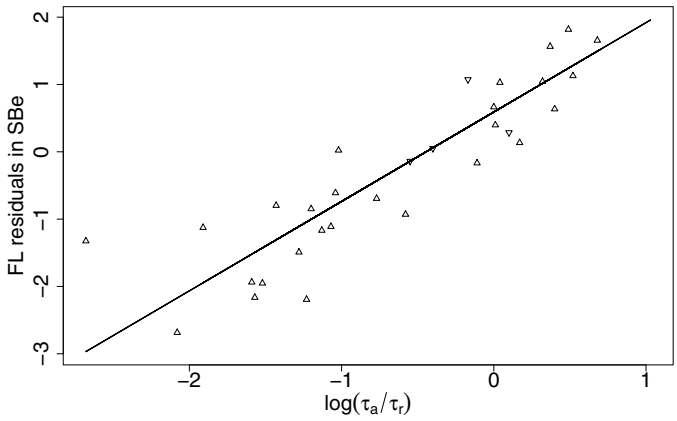

Fig. 7. Trend of residuals to the SB_e-$\log R_e$ relation with cluster age in units of the cluster half-light relaxation time. Only clusters younger than 4 Gyr are shown in the plot. Upwards facing triangles are LMC clusters, downwards facing triangles are SMC clusters. The superimposed line is obtained by performing a least squares linear regression.

opposed to 1.04 mag for the scatter about the relation given by Eq. (4) for the whole sample. The presence of a greater scatter and the indication that it is driven by a third parameter clearly infers that the behavior of young clusters and old clusters in the ($\log R_e$, SB_e) plane is different. Moreover, Fig. 5 shows that old GCs are not located along the extrapolation of the correlation line for the younger clusters. While a firm conclusion regarding this matter would require additional studies, this occurrence may be an indication that massive clusters that are in the SMC, LMC, and Fornax now, are either not similar to the young massive clusters that were the progenitors of the old GCs, or that evolutionary phenomena capable of explaining the non-linearity observed in Fig. 5 are at work.

3.4. Passive stellar evolution or dynamical aging?

The trend of the residuals to the fitted SB_e-$\log R_e$ relation with cluster age may be produced by the evolution of the cluster stellar population with age, whose characteristic timescales are influenced by cluster metallicity but do not display large variations from one cluster to another, or from dynamical effects, e.g., mass loss due to evaporation of light stars. To decouple the dynamical effects from stellar evolution, we studied the dependence of the residuals from the SB_e-$\log R_e$ relation on the ratio τ_a/τ_r of cluster age τ_a to the half-light relaxation time τ_r. The timescale for cluster dissolution by the evaporation of stars is a multiple of τ_r, as well as the timescale for the onset of core-collapse and mass segregation. The ratio τ_a/τ_r is therefore a measure of *dynamical age*, i.e., of how much a cluster has evolved by two-body relaxation processes.

Figure 7 shows a scatter plot of the residuals against τ_a/τ_r. Only clusters younger than 4 Gyr are included in the plot. The trend shown here is stronger than the correlation of residuals with cluster age alone (not shown). The correlation coefficient for clusters younger than 4 Gyr is $r = 0.90$, which is quite tight, even though it remains consistent within its 95% confidence interval with the value of $r = 0.79$ found for the correlation with age alone. This finding suggests that, for young clusters, internal two-body relaxation phenomena play an important role in driving the evolution of the SB_e-$\log R_e$ relation.

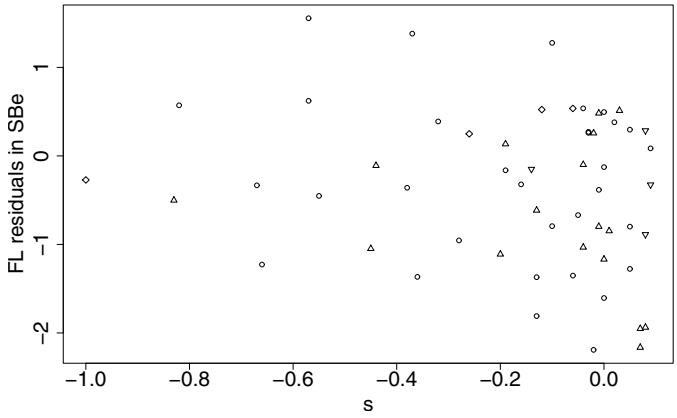

Fig. 8. Scatter plot of the residuals to the SB_e-$\log R_e$ relation versus Noyola & Gebhardt (2006, 2007) central surface brightness profile slope s. Open circles are Galactic GCs, upwards facing triangles are LMC clusters, downwards facing triangles are SMC clusters, and diamonds are Fornax clusters.

3.5. Residuals and the central slope of the surface brightness profile

Figure 8 shows that there is no apparent correlation between residuals of the SB_e-$\log R_e$ relation and central surface brightness profile slopes measured by Noyola & Gebhardt (2006, 2007). The correlation coefficient that we find is $r = -0.19$, which is not significant (with a p-value of 0.16), i.e., r is compatible with 0 and no correlation is present. This result is somewhat unexpected, given the correlation found in Paper I between central surface brightness profile slope and residuals to the fundamental plane of GCs. A possible interpretation is that this correlation is caused by phenomena pertaining to the velocity dispersion σ. This would be the case if the presence of a cusp in the cluster luminosity density profile makes σ higher than expected from the fundamental plane relation.

3.6. Dynamical influence of the galactic environment

To measure environmental effects on the SB_e-$\log R_e$ relation, we study how the residuals vary with different indicators. To quantify the amount of influence that the galactic environment exerts on a sample of 114 GCs, we use distances from the center of

each cluster's host galaxy, listed by McLaughlin & van der Marel (2005).

We find no significant trend of residuals to the SB_e-$\log R_e$ relation with log distance from the host galaxy center. A positive correlation coefficient of $r = 0.22$ is found, which corresponds to a t-test p-value of 0.02.

For the sample of 61 Galactic GCs for which we calculated the radii of the relevant Roche lobes, we find a negative correlation coefficient with the residuals of the SB_e-$\log R_e$ relation, which is marginally significant with 0.01 p-value. In the case of LMC clusters, no significant trend with tidal radii is found.

For the 48 Galactic GCs whose orbits were computed by Allen et al. (2006), the interaction with Galactic environment can be quantified in a more refined way, by using the computed orbital parameters. Allen et al. (2006) calculated their orbits over a period of several Gyr, and list average values of perigalactic distance and orbital eccentricity during this time. These two orbital parameters are understood to set the cluster tidal cutoff radii (e.g., see King 1962), thereby influencing the whole cluster density and surface brightness profile. Surprisingly, we find no correlation between the residuals and either perigalactic distance or orbital eccentricity. The correlation coefficients are consistent with 0 having p-values of 0.19 and 0.30, respectively.

Allen et al. (2006) also computed GC destruction rates relative to the tidal interaction with either the Galactic bulge or the disk. Destruction rates depend on the computed GC orbit as well as the assumed Galactic potential model. Our results are similar for the two potential models considered by the authors of the above paper. We consider the ratio of GC age to the related timescales to measure the amount of environment-driven dynamical evolution. A scatter plot of the residuals[4] of the SB_e-$\log R_e$ relation versus the log ratio of cluster age τ_a to Allen et al. (2006) bulge destruction time τ_b and disk destruction time τ_d shows only a mild trend, with correlation coefficients of 0.45 and 0.49, respectively.

3.7. Power-law behavior of surface brightness profiles in the outermost regions

Figure 9 shows the histogram of the best-fit coefficient a for the relation defined by Eq. (1), for the sample of 145 GCs with sufficient-quality surface brightness profiles. The mean and median values of a for the sample are 3.5 and 3.2 respectively. A value of 3 would be expected for partially relaxed models produced by collisionless collapse (Bertin & Stiavelli (1993), see also Trenti & Bertin (2005)). Figure 10 shows a scatter plot of a versus the concentration parameter c; the values of c are taken from McLaughlin & van der Marel (2005) and obtained by fitting King models to the surface brightness profiles. No significant trend emerges from the sample of 121 GCs for which a and c are available.

With the full sample of 145 GCs, we do not identify any trend in the slopes represented by a with either the half-light relaxation time or the ratio of GC age to relaxation time. This is unsurprising, since the surface brightness profiles of most clusters in this sample are not sufficiently extended in terms of the truncation radius (as obtained by fitting King (1966) models to the profile). We then restrict our attention to a sample of 24 GCs with a measured half-light relaxation time and an extended observed surface brightness profile (McLaughlin & van der Marel 2005). Figure 11 shows a trend in power-law exponent a with log half-light relaxation time, which is quantitatively confirmed by a correlation coefficient $r = 0.58$ that is significant to 2×10^{-3}. The trend is mild but points to the existence of a relation between two-body relaxation phenomena and the shape of the outer envelope of GCs.

[4] both computed for an axisymmetric Galactic potential model

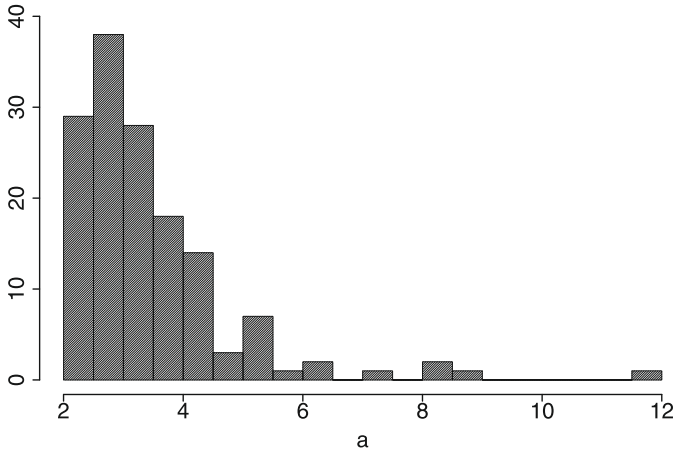

Fig. 9. Histogram of best-fit power law coefficients a for the outer part of the GC surface brightness profiles.

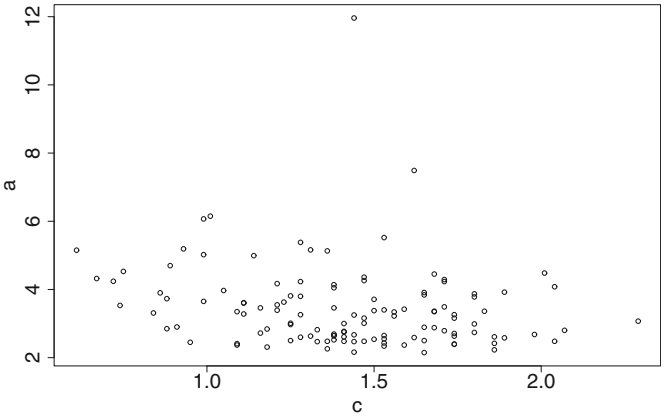

Fig. 10. Scatter plot of power law coefficients a as a function of cluster concentration.

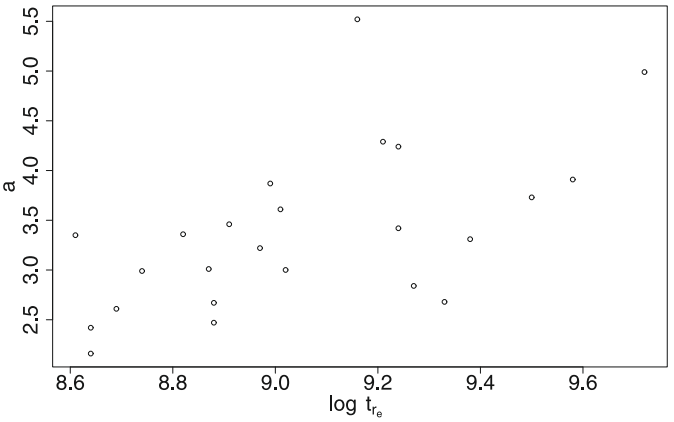

Fig. 11. Correlation of best-fit power law coefficients a for the outer part of GC extended surface brightness profiles with half-light relaxation time by McLaughlin & van der Marel (2005).

4. Discussion and conclusions

By considering a sample of 129 Galactic and extragalactic GCs, we have found a linear relation between SB_e and $\log R_e$, given by Eq. (4). The relevant coefficient 5.25 ± 0.44 is compatible with 5, i.e., with cluster absolute magnitude not showing a systematic linear trend with $\log R_e$. Indeed, when examined in the ($\log R_e$, M_V) plane, the cluster absolute magnitude shows no trend with size (in contrast to the trend exhibited by dwarf spheroidal galaxies; see van den Bergh 2008).

The typical scatter about the relation is 1 mag in SB_e. Young clusters, of age below 4 Gyr, exhibit a larger scatter of about 1.4 mag. GC age seems to be an important factor in driving this scatter, because young clusters are found to display a clear trend of residuals to the relation with age, with a correlation coefficient of $r = 0.79$, while old GCs do not exhibit signs of such a correlation. If we assume that all the massive young clusters included in our sample are genuine GC progenitors, our finding suggests that the scaling law being considered shows signs of evolution with age, i.e., that GCs of different ages differ with respect to this scaling law. Moreover, the larger scatter displayed by young clusters points to an evolutionary origin of the relation between SB_e and $\log R_e$, as opposed to a primordial one. This result is in contrast to the suggestion of Bellazzini (1998) that "at earlier times, globular clusters populated a line in the three-dimensional S-space, i.e., their original dynamical structure was fully determined by a single physical parameter".

In principle, modeling the processes that generate the relation between SB_e and $\log R_e$ would require taking into account passive stellar evolution, internal dynamical phenomena (evaporation and core-collapse driven by two-body relaxation), and dynamical interaction with the environment. We find that the trend with age becomes stronger for young clusters if age is measured in units of the half-light relaxation time of each GC, i.e., if *dynamical age* with respect to two-body relaxation is considered, the correlation coefficient rises to 0.90. Given this result, we argue that two-body relaxation is the key ingredient in shaping the evolution of the SB_e-$\log R_e$ scaling law, at least for young clusters. This may not be the case for older clusters, which do not show such a trend. The evolution of these clusters in the ($\log R_e$, SB_e) plane is likely to be influenced by their host environment, but the available data is of limited use in resolving this issue. The distance to the host galaxy is only a simple proxy for the degree of dynamical disturbance that the GC suffers from it, while more detailed orbital data is available only for a sample of 48 old, Galactic GCs (Allen et al. 2006). In any case, we find no trend between the residuals to the $SB_e - \log R_e$ relation and either distance from the host galaxy or pericenter distance and orbital eccentricity, when these data are available. When GC age is measured in units of the bulge-interaction and disk-interaction destruction times based on the orbital data provided by Allen et al. (2006), weak ($r \approx 0.5$) trends are found with SB_e-$\log R_e$ relation residuals. While this suggests that dynamical interaction with the galactic environment may exert an influence on GCs with observable effects in the ($\log R_e$, SB_e) plane, to draw conclusive evidence, the correlation with age alone should be removed from the trend and a larger sample of clusters with accurately measured orbits is necessary.

In contrast to what we noted for fundamental plane residuals in Paper I, we find here that central surface brightness profile slopes measured by Noyola & Gebhardt (2006) and Noyola & Gebhardt (2007) do not correlate with residuals from the $SB_e - \log R_e$ relation. This result suggests that velocity dispersion information is necessary to understand the mechanism producing cuspy GC surface brightness profiles.

Acknowledgements. We wish to thank S. Degl'Innocenti, W. Harris, M. Lombardi, M. Trenti, E. Vesperini, and D. Kruijssen for their comments and helpful suggestions. This research has made use of the SIMBAD data-base, operated at CDS, Strasbourg, France. Part of this work was carried out at the Kavli Institute for Theoretical Physics, Santa Barbara (CA), while we participated in the Program *Formation and Evolution of Globular Clusters*.

References

Allen, C., Moreno, E., & Pichardo, B. 2006, ApJ, 652, 1150
Barmby, P., McLaughlin, D. E., Harris, W. E., Harris, G. L. H., & Forbes, D. A. 2007, AJ, 133, 2764
Bellazzini, M. 1998, New Astron., 3, 219
Bertin, G., & Stiavelli, M. 1993, Rep. Progr. Phys., 56, 493
Bertin, G., & Varri, A. L. 2008, ApJ, 689, 1005
Carretta, E., & Gratton, R. G. 1997, A&AS, 121, 95
De Angeli, F., Piotto, G., Cassisi, S., et al. 2005, AJ, 130, 116
de Vaucouleurs, G. 1977, in Evolution of Galaxies and Stellar Populations, ed. B. M. Tinsley, & R. B. Larson, 43
Djorgovski, S. 1995, ApJ, 438, L29
Djorgovski, S., & Meylan, G. 1994, AJ, 108, 1292
Ferraro, F. R., Messineo, M., Fusi Pecci, F., et al. 1999, AJ, 118, 1738
Fraser, C. W. 1972, The Observatory, 92, 51
Graham, A. W., Trujillo, I., & Caon, N. 2001, AJ, 122, 1707
Harris, W. E. 1996, AJ, 112, 1487
Heggie, D., & Hut, P. 2003, The Gravitational Million-Body Problem: A Multidisciplinary Approach to Star Cluster Dynamics, ed. P. Heggie, & D. Hut
Holtzman, J. A., Burrows, C. J., Casertano, S., et al. 1995, PASP, 107, 1065
King, I. 1962, AJ, 67, 471
King, I. R. 1966, AJ, 71, 64
Kron, G. E., & Mayall, N. U. 1960, AJ, 65, 581
Kruijssen, J. M. D., & Mieske, S. 2009, A&A, 500, 785
Larsen, S. S. 2004, A&A, 416, 537
Marín-Franch, A., Aparicio, A., Piotto, G., et al. 2009, ApJ, 694, 1498
McLaughlin, D. E., & van der Marel, R. P. 2005, ApJS, 161, 304
Mosteller, F., & Tukey, J. W. 1977, Data analysis and regression: a second course in statistics
Noyola, E., & Gebhardt, K. 2006, AJ, 132, 447
Noyola, E., & Gebhardt, K. 2007, AJ, 134, 912
Pasquato, M., & Bertin, G. 2008, A&A, 489, 1079
Recio-Blanco, A., Piotto, G., de Angeli, F., et al. 2005, A&A, 432, 851
Schweizer, F. 2004, in The Formation and Evolution of Massive Young Star Clusters, ed. H. J. G. L. M. Lamers, L. J. Smith, & A. Nota, ASP Conf. Ser., 322, 111
Spitzer, L. 1987, Dynamical evolution of globular clusters, ed. L. Spitzer
Trager, S. C., King, I. R., & Djorgovski, S. 1995, AJ, 109, 218
Trenti, M., & Bertin, G. 2005, A&A, 429, 161
Trenti, M., Vesperini, E., & Pasquato, M. 2010, ApJ, 708, 1598
van den Bergh, S. 2008, MNRAS, 390, L51
Wilson, C. P. 1975, AJ, 80, 175

Table 1. Adopted photometric quantities.

ID	m	$E(B-V)$	$M-m_0$	$\log r_e$	^{a}
ARP 2	12.74 ± 0.03	0.11 ± 0.011	17.37 ± 0.18	2.1 ± 0.02	2.85
FORNAX 1	15.44 ± 0.08	0.071 ± 0.007	20.68 ± 0.22	1.24 ± 0.06	5.15
FORNAX 2	13.64 ± 0.06	0.054 ± 0.005	20.68 ± 0.22	1.07 ± 0.05	3.31
FORNAX 3	12.73 ± 0.09	0.035 ± 0.004	20.68 ± 0.21	0.85 ± 0.11	7.49
FORNAX 4	13.56 ± 0.13	0.14 ± 0.014	20.68 ± 0.24	0.78 ± 0.15	3.01
FORNAX 5	13.52 ± 0.08	0.031 ± 0.003	20.68 ± 0.21	0.83 ± 0.09	3.78
IC 4499	9.91 ± 0.02	0.175 ± 0.013	16.53 ± 0.1	2.04 ± 0.02	4.17
LMC-HODGE 11	11.24 ± 0.06	0.046 ± 0.005	18.5 ± 0.21	1.49 ± 0.05	3.81
LMC-HODGE 14	12.88 ± 0.14	0.105 ± 0.01	18.5 ± 0.23	1.38 ± 0.16	3.34
LMC-NGC 1466	11.18 ± 0.04	0.09 ± 0.009	18.43 ± 0.1	1.3 ± 0.03	3.28
LMC-NGC 1711	9.57 ± 0.06	0.002 ± 0.001	18.5 ± 0.2	1.36 ± 0.07	3.25
LMC-NGC 1754	11.47 ± 0.07	0.096 ± 0.01	18.5 ± 0.23	1.19 ± 0.09	2.71
LMC-NGC 1777	11.44 ± 0.06	0 ± 0.001	18.5 ± 0.2	1.53 ± 0.05	3.26
LMC-NGC 1786	10.48 ± 0.06	0.125 ± 0.012	18.5 ± 0.24	1.26 ± 0.07	2.15
LMC-NGC 1805	10.29 ± 0.07	0.144 ± 0.014	18.5 ± 0.24	1.2 ± 0.08	2.6
LMC-NGC 1818	9.25 ± 0.07	0.15 ± 0.015	18.5 ± 0.25	1.38 ± 0.08	2.77
LMC-NGC 1831	10.4 ± 0.05	0.104 ± 0.01	18.5 ± 0.23	1.52 ± 0.04	2.84
LMC-NGC 1835	9.94 ± 0.04	0.105 ± 0.01	18.5 ± 0.23	1.02 ± 0.04	2.47
LMC-NGC 1847	10.01 ± 0.13	0.165 ± 0.016	18.5 ± 0.25	1.73 ± 0.13	3.07
LMC-NGC 1850	8.42 ± 0.1	0.102 ± 0.01	18.5 ± 0.23	1.59 ± 0.11	4.23
LMC-NGC 1856	9.28 ± 0.1	0.228 ± 0.023	18.5 ± 0.27	1.5 ± 0.11	3.16
LMC-NGC 1868	11.23 ± 0.05	0.132 ± 0.013	18.5 ± 0.24	1.18 ± 0.05	2.48
LMC-NGC 1898	10.91 ± 0.07	0.083 ± 0.008	18.5 ± 0.23	1.44 ± 0.09	4.36
LMC-NGC 1916	10.17 ± 0.04	0.188 ± 0.019	18.5 ± 0.26	0.97 ± 0.04	4.26
LMC-NGC 2004	9.15 ± 0.09	0.117 ± 0.012	18.5 ± 0.24	1.33 ± 0.12	3.84
LMC-NGC 2005	10.92 ± 0.08	0.12 ± 0.012	18.5 ± 0.24	1.07 ± 0.09	2.34
LMC-NGC 2011	9.76 ± 0.14	0.045 ± 0.004	18.5 ± 0.21	1.42 ± 0.14	4.08
LMC-NGC 2019	10.59 ± 0.07	0.138 ± 0.014	18.5 ± 0.24	1.09 ± 0.1	3.36
LMC-NGC 2031	10.05 ± 0.08	0.119 ± 0.012	18.5 ± 0.24	1.6 ± 0.09	3.38
LMC-NGC 2100	9.2 ± 0.08	0.208 ± 0.021	18.5 ± 0.26	1.31 ± 0.11	3.26
LMC-NGC 2121	11.02 ± 0.12	0.122 ± 0.012	18.5 ± 0.24	1.67 ± 0.08	4.32
LMC-NGC 2136	10.34 ± 0.08	0.189 ± 0.019	18.5 ± 0.26	1.17 ± 0.07	2.5
LMC-NGC 2153	13.11 ± 0.3	0.028 ± 0.003	18.5 ± 0.21	1.01 ± 0.32	11.96
LMC-NGC 2155	11.68 ± 0.1	0.079 ± 0.008	18.5 ± 0.22	1.63 ± 0.09	2.45
LMC-NGC 2157	9.56 ± 0.06	0.098 ± 0.01	18.5 ± 0.23	1.42 ± 0.08	2.67
LMC-NGC 2159	10.74 ± 0.13	0.188 ± 0.019	18.5 ± 0.26	1.5 ± 0.19	2.16
LMC-NGC 2162	12.32 ± 0.11	0.012 ± 0.001	18.5 ± 0.2	1.31 ± 0.1	5.38
LMC-NGC 2172	11.08 ± 0.12	0.092 ± 0.009	18.5 ± 0.23	1.52 ± 0.15	2.26
LMC-NGC 2173	11.53 ± 0.09	0.108 ± 0.011	18.5 ± 0.23	1.62 ± 0.09	2.65
LMC-NGC 2193	12.53 ± 0.23	0.044 ± 0.004	18.5 ± 0.21	1.39 ± 0.24	2.48
LMC-NGC 2210	10.75 ± 0.05	0.096 ± 0.01	18.5 ± 0.23	1.17 ± 0.04	3.61
LMC-NGC 2213	11.92 ± 0.12	0.021 ± 0.002	18.5 ± 0.21	1.34 ± 0.13	2.48
LMC-NGC 2214	10.05 ± 0.09	0.018 ± 0.002	18.5 ± 0.21	1.6 ± 0.13	2.63
LMC-NGC 2231	12.12 ± 0.15	0.106 ± 0.011	18.5 ± 0.23	1.48 ± 0.12	5.13
LMC-NGC 2249	11.9 ± 0.15	0.052 ± 0.005	18.5 ± 0.22	1.21 ± 0.13	3.55
LMC-NGC 2257	11.33 ± 0.07	0 ± 0.001	18.5 ± 0.2	1.7 ± 0.04	2.9
LMC-SL 842	13.42 ± 0.22	0.104 ± 0.01	18.5 ± 0.23	1.25 ± 0.17	6.15
NGC 104	4 ± 0.01	0.04 ± 0.003	13.29 ± 0.06	2.23 ± 0.02	4.48
NGC 1261	8.62 ± 0.02	0.012 ± 0.001	16.01 ± 0.05	1.62 ± 0.02	3.46
NGC 1851	7.24 ± 0.04	0.02 ± 0.001	15.42 ± 0.05	1.51 ± 0.05	2.42
NGC 1904	8.08 ± 0.02	0.01 ± 0.001	15.64 ± 0.05	1.62 ± 0.02	2.88
NGC 2808	6.38 ± 0.01	0.164 ± 0.012	15.09 ± 0.1	1.65 ± 0.01	3.22
NGC 288	8.21 ± 0.02	0.03 ± 0.003	14.67 ± 0.11	2.13 ± 0.01	6.07
NGC 3201	7.07 ± 0.02	0.227 ± 0.016	13.5 ± 0.1	2.18 ± 0.01	3.8
NGC 362	6.59 ± 0.02	0.004 ± 0.001	14.72 ± 0.07	1.62 ± 0.03	2.99
NGC 4147	10.29 ± 0.02	0.012 ± 0.001	16.4 ± 0.07	1.45 ± 0.02	3.36
NGC 4590	8.29 ± 0.01	0.044 ± 0.003	15.12 ± 0.05	1.93 ± 0.01	3
NGC 5024	7.69 ± 0.01	0.01 ± 0.001	16.35 ± 0.08	1.84 ± 0.01	3.91
NGC 5053	9.66 ± 0.04	0.03 ± 0.003	16.17 ± 0.08	2.21 ± 0.02	4.53
NGC 5272	6.53 ± 0.02	0.01 ± 0.001	14.99 ± 0.05	1.85 ± 0.02	3.92
NGC 5286	7.2 ± 0.01	0.24 ± 0.024	15.25 ± 0.17	1.72 ± 0.02	2.75
NGC 5466	9.48 ± 0.02	0 ± 0.001	16.12 ± 0.1	2.12 ± 0.01	3.73
NGC 5634	9.93 ± 0.02	0.01 ± 0.001	17.17 ± 0.09	1.61 ± 0.02	2.8
NGC 5694	10.12 ± 0.01	0.101 ± 0.007	17.77 ± 0.09	1.38 ± 0.02	2.58
NGC 5824	8.84 ± 0.01	0.128 ± 0.009	17.6 ± 0.08	1.44 ± 0.01	2.68
NGC 5897	8.67 ± 0.02	0.08 ± 0.008	15.61 ± 0.09	2.11 ± 0.01	3.9
NGC 5904	5.86 ± 0.01	0.03 ± 0.002	14.37 ± 0.05	2.04 ± 0.01	4.29
NGC 5986	7.81 ± 0.01	0.27 ± 0.027	15.39 ± 0.16	1.73 ± 0.01	3.63
NGC 6093	7.45 ± 0.01	0.196 ± 0.014	15.05 ± 0.09	1.59 ± 0.01	3.35
NGC 6121	5.67 ± 0.01	0.36 ± 0.036	11.62 ± 0.21	2.48 ± 0.01	2.89
NGC 6139	8.86 ± 0.02	0.72 ± 0.072	15.45 ± 0.3	1.87 ± 0.02	2.23
NGC 6171	8.28 ± 0.01	0.38 ± 0.027	13.81 ± 0.15	2.1 ± 0.01	2.43
NGC 6205	5.89 ± 0.01	0.012 ± 0.001	14.46 ± 0.07	1.99 ± 0.01	5.52
NGC 6218	7.17 ± 0.01	0.189 ± 0.013	13.58 ± 0.16	2.04 ± 0.01	4.23

Table 1. continued.

ID	m	$E(B-V)$	$M-m_0$	$\log r_e$	[a]
NGC 6229	9.56 ± 0.01	0.012 ± 0.001	17.42 ± 0.05	1.35 ± 0.01	3.71
NGC 6254	6.66 ± 0.01	0.28 ± 0.028	13.35 ± 0.19	2.04 ± 0.01	4.05
NGC 6256	11.24 ± 0.02	1.18 ± 0.118	14 ± 0.43	1.68 ± 0.01	3.41
NGC 6266	6.46 ± 0.02	0.5 ± 0.035	14.15 ± 0.2	1.81 ± 0.03	2.79
NGC 6273	6.74 ± 0.01	0.34 ± 0.034	15.05 ± 0.18	1.96 ± 0.01	2.55
NGC 6284	8.7 ± 0.02	0.29 ± 0.029	16.06 ± 0.16	1.7 ± 0.01	2.48
NGC 6287	9.46 ± 0.01	0.66 ± 0.066	14.79 ± 0.27	1.71 ± 0.01	2.64
NGC 6293	7.97 ± 0.02	0.62 ± 0.062	14.22 ± 0.26	1.92 ± 0.02	2.16
NGC 6316	9.02 ± 0.02	0.51 ± 0.051	15.59 ± 0.25	1.74 ± 0.02	2.5
NGC 6325	10.49 ± 0.01	1.03 ± 0.103	14.42 ± 0.39	1.74 ± 0.01	2.3
NGC 6333	7.75 ± 0.01	0.36 ± 0.036	14.62 ± 0.26	1.77 ± 0.01	3.01
NGC 6341	6.56 ± 0.01	0.02 ± 0.002	14.74 ± 0.11	1.75 ± 0.01	4.45
NGC 6342	9.78 ± 0.02	0.46 ± 0.046	14.95 ± 0.22	1.65 ± 0.02	3.15
NGC 6356	8.13 ± 0.01	0.28 ± 0.028	16 ± 0.17	1.79 ± 0.01	2.37
NGC 6362	7.54 ± 0.01	0.08 ± 0.008	14.48 ± 0.11	2.16 ± 0.01	2.37
NGC 6366	8.68 ± 0.01	0.69 ± 0.069	12.88 ± 0.31	2.28 ± 0.01	3.53
NGC 6388	6.87 ± 0.01	0.37 ± 0.037	15.42 ± 0.2	1.51 ± 0.01	3.49
NGC 6397	5.95 ± 0.01	0.18 ± 0.018	11.89 ± 0.16	2.24 ± 0.02	3.14
NGC 6401	9.57 ± 0.02	0.91 ± 0.091	14.55 ± 0.41	1.84 ± 0.02	2.67
NGC 6402	7.73 ± 0.01	0.66 ± 0.066	14.91 ± 0.28	1.91 ± 0.01	3.65
NGC 6440	9.43 ± 0.01	1.09 ± 0.077	14.69 ± 0.32	1.51 ± 0.01	2.59
NGC 6441	7.19 ± 0.03	0.47 ± 0.047	15.77 ± 0.23	1.61 ± 0.04	2.4
NGC 6517	10.54 ± 0.01	1.23 ± 0.123	15.04 ± 0.45	1.58 ± 0.01	2.56
NGC 6522	8.46 ± 0.03	0.54 ± 0.054	14.66 ± 0.25	1.63 ± 0.03	8.3
NGC 6528	9.59 ± 0.06	0.62 ± 0.062	14.35 ± 0.39	1.43 ± 0.05	2.54
NGC 6539	9.64 ± 0.03	0.97 ± 0.097	14.9 ± 0.37	2.06 ± 0.04	2.39
NGC 6553	8.03 ± 0.01	0.84 ± 0.084	13.44 ± 0.46	1.88 ± 0.01	2.72
NGC 6569	8.8 ± 0.02	0.57 ± 0.057	15.26 ± 0.25	1.76 ± 0.02	2.63
NGC 6584	8.93 ± 0.01	0.023 ± 0.002	15.76 ± 0.06	1.71 ± 0.01	3.16
NGC 6624	7.82 ± 0.01	0.28 ± 0.028	14.43 ± 0.18	1.79 ± 0.01	2.25
NGC 6637	7.46 ± 0.01	0.17 ± 0.012	14.7 ± 0.1	1.8 ± 0.01	2.52
NGC 6638	8.89 ± 0.01	0.39 ± 0.039	15.14 ± 0.21	1.53 ± 0.01	2.82
NGC 6642	9.35 ± 0.03	0.44 ± 0.044	14.83 ± 0.22	1.63 ± 0.02	2.59
NGC 6652	8.98 ± 0.02	0.103 ± 0.007	15.01 ± 0.09	1.53 ± 0.01	2.74
NGC 6681	7.93 ± 0.02	0.064 ± 0.005	15 ± 0.08	1.78 ± 0.02	2.44
NGC 6712	8.11 ± 0.03	0.419 ± 0.03	14.27 ± 0.15	1.93 ± 0.03	3.97
NGC 6723	7.24 ± 0.02	0.05 ± 0.005	14.74 ± 0.11	1.95 ± 0.02	3.6
NGC 6752	5.67 ± 0.01	0.04 ± 0.004	13.13 ± 0.16	2.08 ± 0.02	3.84
NGC 6809	6.84 ± 0.01	0.07 ± 0.007	13.78 ± 0.12	2.22 ± 0.02	5.19
NGC 6864	8.52 ± 0.02	0.21 ± 0.021	16.49 ± 0.15	1.44 ± 0.02	3.87
NGC 6934	8.77 ± 0.01	0.09 ± 0.006	16.05 ± 0.08	1.56 ± 0.01	3.4
NGC 6981	9.3 ± 0.02	0.05 ± 0.004	16.1 ± 0.06	1.71 ± 0.02	3.39
NGC 7006	10.63 ± 0.01	0.05 ± 0.005	18.03 ± 0.17	1.41 ± 0.01	2.61
NGC 7078	6.38 ± 0.01	0.09 ± 0.006	15.15 ± 0.08	1.8 ± 0.01	3.18
NGC 7089	6.41 ± 0.01	0.01 ± 0.001	15.47 ± 0.09	1.78 ± 0.01	3.42
NGC 7099	7.57 ± 0.01	0.03 ± 0.002	14.7 ± 0.07	1.8 ± 0.01	2.92
NGC 7492	11.39 ± 0.03	0 ± 0.001	17.1 ± 0.1	1.84 ± 0.02	4.24
SMC-KRON 3	11.1 ± 0.07	0.016 ± 0.002	18.89 ± 0.2	1.59 ± 0.06	4.99
SMC-NGC 121	10.71 ± 0.05	0.146 ± 0.015	18.89 ± 0.25	1.37 ± 0.06	2.31
SMC-NGC 152	11.65 ± 0.08	0.12 ± 0.012	18.89 ± 0.24	1.7 ± 0.06	3.35
SMC-NGC 176	12.21 ± 0.19	0 ± 0.001	18.89 ± 0.2	1.34 ± 0.18	2.97
SMC-NGC 361	11.13 ± 0.09	0.069 ± 0.007	18.89 ± 0.22	1.55 ± 0.06	5.02
SMC-NGC 411	11.61 ± 0.11	0.054 ± 0.005	18.89 ± 0.22	1.42 ± 0.1	2.69
SMC-NGC 416	11.18 ± 0.06	0.127 ± 0.013	18.89 ± 0.24	1.24 ± 0.05	4.7
SMC-NGC 458	11.09 ± 0.09	0.022 ± 0.002	18.89 ± 0.21	1.44 ± 0.07	2.41

Notes. [a] Cluster name. [b] V-band integrated apparent magnitude, this paper, based on model-independent smoothing and integration of Trager et al. (1995) surface brightness profiles, mag. [c] Line-of-sight reddening, Ferraro et al. (1999) and Recio-Blanco et al. (2005) (galactic GCs), Recio-Blanco et al. (2005) (extragalactic clusters), mag. [d] True distance modulus Ferraro et al. (1999) and Recio-Blanco et al. (2005) (galactic GCs), Recio-Blanco et al. (2005) (extragalactic clusters), mag. [e] Log projected angular half-light radius, this paper, based on model-independent smoothing and integration of Trager et al. (1995) surface brightness profiles, arcsec. [f] Slope of the outermost surface brightness profile, this paper, dimensionless.

Table 2. Half-light photometric quantities (*a* and *b*), integrated absolute magnitudes (*c*) and residuals (*d*) to the SB_e-log R_e relation.

ID	SB_e	log R_e	M	Residuals
ARP 2	24.87 ± 0.16	1.26 ± 0.06	−4.97 ± 0.25	2.67
FORNAX 1	23.38 ± 0.4	1.06 ± 0.1	−5.46 ± 0.33	2.23
FORNAX 2	20.83 ± 0.33	0.9 ± 0.09	−7.21 ± 0.29	0.52
FORNAX 3	18.86 ± 0.65	0.68 ± 0.15	−8.06 ± 0.31	−0.27
FORNAX 4	19.03 ± 0.93	0.61 ± 0.2	−7.55 ± 0.42	0.25
FORNAX 5	19.55 ± 0.53	0.65 ± 0.13	−7.26 ± 0.29	0.54
IC 4499	21.55 ± 0.16	1.03 ± 0.04	−7.16 ± 0.16	0.53
LMC-HODGE 11	20.54 ± 0.33	0.88 ± 0.09	−7.4 ± 0.29	0.33
LMC-HODGE 14	21.44 ± 0.97	0.77 ± 0.21	−5.95 ± 0.4	1.82
LMC-NGC 1466	19.39 ± 0.22	0.68 ± 0.05	−7.53 ± 0.17	0.26
LMC-NGC 1711	18.35 ± 0.41	0.75 ± 0.11	−8.94 ± 0.26	−1.17
LMC-NGC 1754	19.13 ± 0.55	0.58 ± 0.14	−7.33 ± 0.33	0.48
LMC-NGC 1777	21.08 ± 0.31	0.92 ± 0.09	−7.06 ± 0.26	0.67
LMC-NGC 1786	18.4 ± 0.45	0.65 ± 0.12	−8.41 ± 0.34	−0.62
LMC-NGC 1805	17.83 ± 0.52	0.59 ± 0.13	−8.66 ± 0.36	−0.85
LMC-NGC 1818	17.67 ± 0.52	0.77 ± 0.13	−9.71 ± 0.36	−1.95
LMC-NGC 1831	19.67 ± 0.28	0.91 ± 0.09	−8.42 ± 0.31	−0.69
LMC-NGC 1835	16.69 ± 0.27	0.41 ± 0.09	−8.89 ± 0.31	−1.03
LMC-NGC 1847	20.13 ± 0.83	1.12 ± 0.18	−9 ± 0.43	−1.33
LMC-NGC 1850	18.04 ± 0.68	0.98 ± 0.16	−10.4 ± 0.36	−2.69
LMC-NGC 1856	18.05 ± 0.72	0.89 ± 0.16	−9.93 ± 0.45	−2.19
LMC-NGC 1868	18.71 ± 0.34	0.57 ± 0.1	−7.68 ± 0.33	0.13
LMC-NGC 1898	19.84 ± 0.55	0.83 ± 0.14	−7.85 ± 0.32	−0.1
LMC-NGC 1916	16.44 ± 0.29	0.36 ± 0.09	−8.91 ± 0.35	−1.05
LMC-NGC 2004	17.42 ± 0.73	0.72 ± 0.17	−9.71 ± 0.36	−1.94
LMC-NGC 2005	17.87 ± 0.57	0.46 ± 0.14	−7.95 ± 0.35	−0.11
LMC-NGC 2011	18.71 ± 0.85	0.81 ± 0.18	−8.88 ± 0.37	−1.13
LMC-NGC 2019	17.58 ± 0.61	0.48 ± 0.15	−8.34 ± 0.36	−0.5
LMC-NGC 2031	19.67 ± 0.57	0.99 ± 0.14	−8.82 ± 0.36	−1.11
LMC-NGC 2100	17.08 ± 0.7	0.7 ± 0.16	−9.95 ± 0.41	−2.16
LMC-NGC 2121	20.98 ± 0.56	1.06 ± 0.13	−7.86 ± 0.4	−0.17
LMC-NGC 2136	17.59 ± 0.49	0.56 ± 0.12	−8.75 ± 0.4	−0.93
LMC-NGC 2153	20.04 ± 1.91	0.4 ± 0.36	−5.48 ± 0.52	2.38
LMC-NGC 2155	21.58 ± 0.58	1.02 ± 0.13	−7.06 ± 0.35	0.64
LMC-NGC 2157	18.35 ± 0.5	0.81 ± 0.13	−9.24 ± 0.33	−1.49
LMC-NGC 2159	19.65 ± 1.13	0.89 ± 0.24	−8.34 ± 0.44	−0.61
LMC-NGC 2162	20.82 ± 0.62	0.7 ± 0.14	−6.22 ± 0.32	1.56
LMC-NGC 2172	20.39 ± 0.9	0.91 ± 0.2	−7.7 ± 0.38	0.02
LMC-NGC 2173	21.28 ± 0.57	1.01 ± 0.14	−7.31 ± 0.35	0.4
LMC-NGC 2193	21.33 ± 1.44	0.78 ± 0.28	−6.11 ± 0.46	1.65
LMC-NGC 2210	18.29 ± 0.28	0.56 ± 0.09	−8.05 ± 0.31	−0.23
LMC-NGC 2213	20.54 ± 0.77	0.73 ± 0.17	−6.65 ± 0.33	1.13
LMC-NGC 2214	19.98 ± 0.75	0.99 ± 0.17	−8.51 ± 0.3	−0.8
LMC-NGC 2231	21.19 ± 0.78	0.87 ± 0.17	−6.71 ± 0.41	1.03
LMC-NGC 2249	19.78 ± 0.82	0.6 ± 0.17	−6.76 ± 0.38	1.04
LMC-NGC 2257	21.83 ± 0.27	1.09 ± 0.08	−7.17 ± 0.27	0.51
LMC-SL 842	21.34 ± 1.1	0.64 ± 0.22	−5.4 ± 0.48	2.39
NGC 104	17.02 ± 0.12	0.58 ± 0.03	−9.42 ± 0.08	−1.6
NGC 1261	18.67 ± 0.12	0.51 ± 0.03	−7.43 ± 0.07	0.4
NGC 1851	16.72 ± 0.29	0.29 ± 0.06	−8.24 ± 0.09	−0.36
NGC 1904	18.12 ± 0.13	0.43 ± 0.03	−7.59 ± 0.08	0.26
NGC 2808	16.11 ± 0.1	0.36 ± 0.03	−9.22 ± 0.14	−1.35
NGC 288	20.78 ± 0.08	0.76 ± 0.03	−6.55 ± 0.14	1.21
NGC 3201	19.25 ± 0.12	0.57 ± 0.03	−7.13 ± 0.17	0.68
NGC 362	16.67 ± 0.17	0.25 ± 0.04	−8.15 ± 0.09	−0.25
NGC 4147	19.51 ± 0.12	0.42 ± 0.03	−6.15 ± 0.08	1.7
NGC 4590	19.81 ± 0.07	0.65 ± 0.02	−6.97 ± 0.07	0.82
NGC 5024	18.82 ± 0.07	0.8 ± 0.03	−8.69 ± 0.1	−0.94
NGC 5053	22.63 ± 0.15	1.14 ± 0.04	−6.6 ± 0.13	1.07
NGC 5272	17.73 ± 0.12	0.54 ± 0.03	−8.49 ± 0.07	−0.67
NGC 5286	17.05 ± 0.19	0.46 ± 0.05	−8.79 ± 0.26	−0.95
NGC 5466	22.06 ± 0.07	1.03 ± 0.03	−6.64 ± 0.12	1.06
NGC 5634	19.92 ± 0.12	0.73 ± 0.04	−7.27 ± 0.11	0.5
NGC 5694	18.69 ± 0.14	0.62 ± 0.04	−7.96 ± 0.12	−0.16
NGC 5824	17.65 ± 0.09	0.65 ± 0.03	−9.16 ± 0.12	−1.37
NGC 5897	20.96 ± 0.1	0.92 ± 0.03	−7.19 ± 0.14	0.54
NGC 5904	17.95 ± 0.07	0.6 ± 0.02	−8.6 ± 0.07	−0.8
NGC 5986	17.6 ± 0.14	0.5 ± 0.04	−8.41 ± 0.25	−0.58
NGC 6093	16.77 ± 0.11	0.29 ± 0.03	−8.2 ± 0.15	−0.32
NGC 6121	18.97 ± 0.17	0.5 ± 0.05	−7.07 ± 0.33	0.76
NGC 6139	17.97 ± 0.34	0.65 ± 0.08	−8.82 ± 0.54	−1.03
NGC 6171	19.61 ± 0.15	0.56 ± 0.04	−6.71 ± 0.25	1.11
NGC 6205	17.79 ± 0.06	0.57 ± 0.02	−8.61 ± 0.09	−0.79
NGC 6218	18.8 ± 0.1	0.45 ± 0.04	−7 ± 0.21	0.85

Table 2. continued.

ID	SB_e	$\log R_e$	M	Residuals
NGC 6229	18.25 ± 0.07	0.52 ± 0.02	−7.9 ± 0.06	−0.08
NGC 6254	18 ± 0.15	0.4 ± 0.05	−7.56 ± 0.29	0.3
NGC 6256	17.99 ± 0.43	0.17 ± 0.1	−6.42 ± 0.82	1.5
NGC 6266	15.95 ± 0.28	0.33 ± 0.07	−9.24 ± 0.33	−1.37
NGC 6273	17.47 ± 0.17	0.66 ± 0.05	−9.37 ± 0.3	−1.58
NGC 6284	18.28 ± 0.16	0.6 ± 0.04	−8.26 ± 0.27	−0.45
NGC 6287	17.94 ± 0.27	0.36 ± 0.06	−7.37 ± 0.49	0.49
NGC 6293	17.63 ± 0.31	0.45 ± 0.07	−8.17 ± 0.47	−0.33
NGC 6316	18.12 ± 0.28	0.55 ± 0.07	−8.15 ± 0.43	−0.33
NGC 6325	17.98 ± 0.38	0.31 ± 0.09	−7.13 ± 0.72	0.75
NGC 6333	17.46 ± 0.17	0.38 ± 0.06	−7.99 ± 0.39	−0.13
NGC 6341	17.23 ± 0.06	0.39 ± 0.03	−8.24 ± 0.12	−0.38
NGC 6342	18.58 ± 0.26	0.33 ± 0.06	−6.59 ± 0.38	1.28
NGC 6356	18.19 ± 0.09	0.68 ± 0.03	−8.74 ± 0.26	−0.95
NGC 6362	20.07 ± 0.09	0.74 ± 0.03	−7.19 ± 0.15	0.58
NGC 6366	19.94 ± 0.27	0.55 ± 0.07	−6.34 ± 0.53	1.48
NGC 6388	15.26 ± 0.17	0.28 ± 0.05	−9.69 ± 0.32	−1.81
NGC 6397	18.58 ± 0.17	0.31 ± 0.05	−6.5 ± 0.23	1.38
NGC 6401	17.93 ± 0.4	0.44 ± 0.1	−7.8 ± 0.72	0.04
NGC 6402	17.22 ± 0.22	0.58 ± 0.06	−9.22 ± 0.5	−1.41
NGC 6440	15.61 ± 0.3	0.14 ± 0.07	−8.64 ± 0.57	−0.72
NGC 6441	15.78 ± 0.37	0.46 ± 0.09	−10.03 ± 0.4	−2.19
NGC 6517	16.6 ± 0.44	0.28 ± 0.1	−8.32 ± 0.84	−0.43
NGC 6522	16.93 ± 0.35	0.25 ± 0.08	−7.88 ± 0.44	0.01
NGC 6528	16.8 ± 0.5	−0.01 ± 0.13	−6.68 ± 0.64	1.28
NGC 6539	18.92 ± 0.53	0.73 ± 0.11	−8.26 ± 0.7	−0.49
NGC 6553	16.81 ± 0.32	0.26 ± 0.1	−8.01 ± 0.73	−0.12
NGC 6569	17.81 ± 0.3	0.5 ± 0.07	−8.22 ± 0.44	−0.39
NGC 6584	19.4 ± 0.07	0.55 ± 0.02	−6.9 ± 0.08	0.92
NGC 6624	17.88 ± 0.15	0.36 ± 0.05	−7.48 ± 0.28	0.39
NGC 6637	17.92 ± 0.1	0.43 ± 0.03	−7.76 ± 0.15	0.08
NGC 6638	17.31 ± 0.18	0.24 ± 0.05	−7.46 ± 0.34	0.44
NGC 6642	18.12 ± 0.26	0.28 ± 0.06	−6.85 ± 0.38	1.04
NGC 6652	18.3 ± 0.09	0.22 ± 0.03	−6.35 ± 0.12	1.55
NGC 6681	18.64 ± 0.13	0.47 ± 0.04	−7.27 ± 0.11	0.57
NGC 6712	18.47 ± 0.28	0.48 ± 0.06	−7.46 ± 0.27	0.38
NGC 6723	18.82 ± 0.14	0.59 ± 0.04	−7.66 ± 0.16	0.15
NGC 6752	17.94 ± 0.12	0.4 ± 0.05	−7.58 ± 0.19	0.27
NGC 6809	19.72 ± 0.14	0.67 ± 0.04	−7.16 ± 0.16	0.63
NGC 6864	17.06 ± 0.18	0.43 ± 0.05	−8.62 ± 0.23	−0.77
NGC 6934	18.27 ± 0.08	0.46 ± 0.03	−7.56 ± 0.11	0.28
NGC 6981	19.68 ± 0.13	0.62 ± 0.03	−6.95 ± 0.09	0.85
NGC 7006	19.51 ± 0.08	0.71 ± 0.04	−7.56 ± 0.19	0.22
NGC 7078	17.08 ± 0.08	0.52 ± 0.03	−9.05 ± 0.11	−1.23
NGC 7089	17.26 ± 0.06	0.56 ± 0.03	−9.09 ± 0.1	−1.28
NGC 7099	18.47 ± 0.07	0.43 ± 0.02	−7.22 ± 0.09	0.62
NGC 7492	22.57 ± 0.13	0.95 ± 0.04	−5.71 ± 0.13	2.01
SMC-KRON 3	21 ± 0.37	1.06 ± 0.1	−7.84 ± 0.28	−0.15
SMC-NGC 121	19.1 ± 0.4	0.84 ± 0.11	−8.63 ± 0.34	−0.89
SMC-NGC 152	21.77 ± 0.42	1.17 ± 0.11	−7.61 ± 0.36	0.05
SMC-NGC 176	20.9 ± 1.09	0.81 ± 0.22	−6.68 ± 0.39	1.07
SMC-NGC 361	20.67 ± 0.41	1.02 ± 0.1	−7.97 ± 0.33	−0.27
SMC-NGC 411	20.53 ± 0.62	0.89 ± 0.14	−7.45 ± 0.34	0.29
SMC-NGC 416	18.98 ± 0.35	0.71 ± 0.1	−8.1 ± 0.34	−0.33
SMC-NGC 458	20.21 ± 0.45	0.91 ± 0.11	−7.87 ± 0.3	−0.14

Notes. [(a)] Average V-band surface brightness within the half-light radius, this paper, mag/arcsec^2. [(b)] Projected half-light radius, this paper, parsec. [(c)] V-band integrated absolute magnitude, this paper, mag. [(d)] Residuals in SB_e to the $SB_e - \log R_e$ relation, this paper, mag/arcsec^2.

Table 3. Catalogue of projected fraction-of-light radii (in arcsec) obtained by using the model-independent method presented in Paper I.

ID	$\log r_{10\%}$	$\log r_{20\%}$	$\log r_{30\%}$	$\log r_{40\%}$	$\log r_{60\%}$	$\log r_{70\%}$	$\log r_{80\%}$	$\log r_{90\%}$
ARP 2	1.607	1.777	1.897	1.997	2.197	2.307	2.437	2.607
FORNAX 1	0.785	0.965	1.075	1.155	1.315	1.385	1.475	1.595
FORNAX 2	0.574	0.754	0.874	0.974	1.164	1.274	1.404	1.614
FORNAX 3	0.250	0.430	0.580	0.710	0.980	1.130	1.310	1.560
FORNAX 4	0.213	0.383	0.523	0.653	0.913	1.073	1.263	1.553
FORNAX 5	0.207	0.387	0.547	0.687	0.967	1.117	1.317	1.587
IC 1276	1.663	1.863	2.003	2.133	2.383	2.543	2.773	3.263
IC 4499	1.489	1.699	1.829	1.939	2.139	2.229	2.339	2.489
LMC-HODGE 11	0.920	1.120	1.260	1.380	1.590	1.700	1.810	1.930
LMC-HODGE 14	0.749	0.959	1.109	1.249	1.519	1.669	1.819	2.039
LMC-NGC 1466	0.760	0.960	1.090	1.190	1.400	1.510	1.650	1.850
LMC-NGC 1711	0.790	0.970	1.110	1.230	1.500	1.670	1.860	2.100
LMC-NGC 1754	0.553	0.733	0.893	1.043	1.363	1.543	1.763	2.073
LMC-NGC 1777	0.950	1.150	1.300	1.410	1.640	1.750	1.900	2.090
LMC-NGC 1786	0.704	0.864	1.004	1.134	1.424	1.644	1.954	2.424
LMC-NGC 1805	0.579	0.779	0.929	1.059	1.359	1.569	1.809	2.109
LMC-NGC 1818	0.800	1.000	1.140	1.260	1.500	1.650	1.830	2.130
LMC-NGC 1831	1.011	1.191	1.311	1.421	1.631	1.741	1.881	2.151
LMC-NGC 1835	0.448	0.648	0.788	0.908	1.138	1.278	1.528	2.028
LMC-NGC 1847	0.979	1.239	1.439	1.599	1.859	1.989	2.119	2.239
LMC-NGC 1850	0.940	1.170	1.320	1.460	1.740	1.890	2.050	2.210
LMC-NGC 1856	0.818	1.048	1.218	1.368	1.638	1.778	1.928	2.128
LMC-NGC 1868	0.609	0.809	0.939	1.059	1.299	1.439	1.639	2.009
LMC-NGC 1898	0.830	1.030	1.180	1.310	1.580	1.720	1.840	1.980
LMC-NGC 1916	0.442	0.602	0.732	0.852	1.092	1.232	1.412	1.662
LMC-NGC 2004	0.719	0.909	1.059	1.189	1.489	1.659	1.869	2.109
LMC-NGC 2005	0.356	0.586	0.756	0.916	1.236	1.436	1.696	2.056
LMC-NGC 2011	0.680	0.930	1.130	1.280	1.550	1.670	1.790	1.920
LMC-NGC 2019	0.396	0.616	0.786	0.936	1.276	1.506	1.776	2.066
LMC-NGC 2031	0.950	1.160	1.320	1.470	1.720	1.840	1.970	2.160
LMC-NGC 2100	0.608	0.838	1.008	1.158	1.458	1.638	1.858	2.108
LMC-NGC 2121	1.209	1.379	1.499	1.589	1.739	1.819	1.909	2.029
LMC-NGC 2136	0.630	0.820	0.950	1.060	1.280	1.410	1.620	2.010
LMC-NGC 2153	0.386	0.606	0.756	0.886	1.126	1.246	1.396	1.576
LMC-NGC 2155	1.020	1.230	1.370	1.510	1.760	1.900	2.040	2.180
LMC-NGC 2157	0.830	1.020	1.150	1.270	1.610	1.880	2.260	2.520
LMC-NGC 2159	0.850	1.040	1.190	1.330	1.730	1.990	2.330	2.530
LMC-NGC 2162	0.760	0.960	1.100	1.210	1.420	1.520	1.640	1.780
LMC-NGC 2172	0.890	1.080	1.220	1.360	1.710	1.950	2.180	2.400
LMC-NGC 2173	0.960	1.180	1.340	1.490	1.760	1.910	2.110	2.380
LMC-NGC 2193	0.699	0.929	1.089	1.239	1.539	1.719	1.919	2.149
LMC-NGC 2210	0.670	0.850	0.970	1.070	1.270	1.390	1.550	1.800
LMC-NGC 2213	0.709	0.919	1.069	1.199	1.499	1.689	1.939	2.249
LMC-NGC 2214	0.880	1.110	1.280	1.430	1.760	1.930	2.140	2.480
LMC-NGC 2231	0.901	1.131	1.271	1.381	1.571	1.651	1.751	1.871
LMC-NGC 2249	0.650	0.850	0.990	1.110	1.320	1.440	1.590	1.800
LMC-NGC 2257	1.173	1.363	1.493	1.603	1.803	1.893	1.983	2.073
LMC-SL 842	0.780	0.950	1.070	1.160	1.330	1.430	1.540	1.700
NGC 104	1.440	1.720	1.920	2.090	2.380	2.540	2.690	2.890
NGC 1261	1.100	1.300	1.430	1.530	1.710	1.810	1.940	2.130
NGC 1851	0.731	1.001	1.201	1.351	1.681	1.871	2.141	2.551
NGC 1904	0.967	1.197	1.357	1.497	1.747	1.887	2.057	2.327
NGC 2419	0.860	1.110	1.280	1.410	1.650	1.770	1.920	2.130
NGC 2808	1.070	1.280	1.420	1.540	1.750	1.860	2.000	2.250
NGC 288	1.654	1.854	1.964	2.054	2.204	2.294	2.384	2.504
NGC 3201	1.638	1.818	1.958	2.068	2.278	2.388	2.528	2.718
NGC 362	0.970	1.200	1.350	1.490	1.760	1.920	2.090	2.340
NGC 4147	0.743	1.033	1.193	1.333	1.573	1.713	1.873	2.093
NGC 4590	1.374	1.574	1.704	1.824	2.044	2.174	2.324	2.594
NGC 5024	1.235	1.445	1.595	1.725	1.955	2.095	2.275	2.495
NGC 5053	1.795	1.965	2.065	2.145	2.285	2.355	2.445	2.575
NGC 5139	1.948	2.138	2.258	2.358	2.538	2.638	2.748	2.888
NGC 5272	1.289	1.479	1.619	1.739	1.969	2.089	2.229	2.479
NGC 5286	1.100	1.320	1.470	1.600	1.850	1.990	2.180	2.460
NGC 5466	1.678	1.828	1.938	2.028	2.198	2.278	2.378	2.528
NGC 5634	0.857	1.127	1.307	1.457	1.757	1.917	2.107	2.417
NGC 5694	0.618	0.878	1.068	1.228	1.528	1.708	1.918	2.218
NGC 5824	0.613	0.873	1.073	1.253	1.633	1.853	2.093	2.443
NGC 5897	1.650	1.820	1.930	2.030	2.200	2.280	2.380	2.540
NGC 5904	1.359	1.589	1.759	1.909	2.169	2.289	2.419	2.599
NGC 5986	1.238	1.418	1.538	1.638	1.828	1.928	2.048	2.228
NGC 6093	0.898	1.128	1.308	1.448	1.708	1.828	1.968	2.178
NGC 6121	1.805	2.065	2.235	2.365	2.595	2.725	2.885	3.165
NGC 6139	1.020	1.310	1.520	1.700	2.050	2.260	2.500	2.810

Table 3. continued.

ID	log $r_{10\%}$	log $r_{20\%}$	log $r_{30\%}$	log $r_{40\%}$	log $r_{60\%}$	log $r_{70\%}$	log $r_{80\%}$	log $r_{90\%}$
NGC 6171	1.434	1.664	1.834	1.974	2.254	2.414	2.624	2.924
NGC 6205	1.449	1.649	1.779	1.889	2.089	2.199	2.309	2.479
NGC 6218	1.494	1.704	1.844	1.944	2.134	2.234	2.344	2.494
NGC 6229	0.757	0.967	1.117	1.237	1.467	1.577	1.717	1.907
NGC 6254	1.484	1.674	1.814	1.934	2.164	2.284	2.414	2.594
NGC 6256	1.094	1.334	1.484	1.594	1.774	1.854	1.924	2.004
NGC 6266	1.130	1.370	1.530	1.670	1.940	2.090	2.270	2.560
NGC 6273	1.328	1.548	1.698	1.828	2.098	2.258	2.468	2.798
NGC 6284	0.988	1.238	1.418	1.568	1.838	2.008	2.178	2.358
NGC 6287	1.138	1.348	1.488	1.598	1.828	1.978	2.148	2.398
NGC 6293	1.098	1.388	1.588	1.758	2.088	2.278	2.478	2.698
NGC 6316	0.988	1.238	1.428	1.588	1.868	2.018	2.238	2.698
NGC 6325	1.048	1.278	1.468	1.608	1.878	2.048	2.248	2.528
NGC 6333	1.227	1.417	1.547	1.657	1.877	2.007	2.167	2.417
NGC 6341	1.129	1.349	1.499	1.639	1.869	1.999	2.139	2.319
NGC 6342	0.937	1.197	1.387	1.527	1.807	1.927	2.057	2.267
NGC 6356	1.117	1.337	1.507	1.647	1.927	2.097	2.327	2.737
NGC 6362	1.608	1.788	1.918	2.038	2.308	2.488	2.698	2.968
NGC 6366	1.802	1.982	2.102	2.202	2.362	2.452	2.562	2.742
NGC 6388	0.870	1.100	1.250	1.390	1.640	1.770	1.930	2.150
NGC 6397	1.580	1.800	1.960	2.110	2.380	2.520	2.690	2.940
NGC 6401	1.148	1.388	1.568	1.708	1.948	2.068	2.198	2.338
NGC 6402	1.409	1.589	1.709	1.819	1.999	2.099	2.219	2.399
NGC 6440	0.834	1.074	1.234	1.374	1.654	1.814	2.024	2.324
NGC 6441	0.882	1.112	1.292	1.452	1.782	1.972	2.212	2.572
NGC 6517	0.827	1.107	1.297	1.447	1.717	1.867	2.057	2.337
NGC 6522	0.950	1.200	1.380	1.510	1.740	1.840	1.930	2.020
NGC 6528	0.798	1.008	1.168	1.298	1.568	1.728	1.958	2.298
NGC 6539	1.389	1.609	1.769	1.909	2.219	2.419	2.659	2.969
NGC 6541	1.120	1.360	1.540	1.690	1.990	2.160	2.380	2.740
NGC 6553	1.328	1.528	1.658	1.768	1.988	2.108	2.288	2.598
NGC 6569	1.158	1.368	1.508	1.638	1.888	2.038	2.238	2.638
NGC 6584	1.130	1.340	1.480	1.600	1.820	1.930	2.060	2.210
NGC 6624	0.968	1.258	1.458	1.628	1.948	2.128	2.308	2.498
NGC 6626	1.208	1.468	1.648	1.808	2.128	2.328	2.598	3.048
NGC 6637	1.160	1.380	1.530	1.670	1.940	2.100	2.300	2.590
NGC 6638	0.937	1.137	1.277	1.407	1.657	1.797	1.977	2.227
NGC 6642	0.858	1.138	1.338	1.488	1.748	1.878	1.988	2.108
NGC 6652	0.820	1.080	1.260	1.400	1.660	1.810	2.000	2.270
NGC 6656	1.758	1.968	2.118	2.258	2.518	2.678	2.858	3.128
NGC 6681	0.983	1.273	1.463	1.623	1.943	2.123	2.343	2.733
NGC 6712	1.384	1.564	1.704	1.824	2.034	2.114	2.214	2.354
NGC 6715	0.790	1.030	1.210	1.370	1.690	1.890	2.150	2.550
NGC 6723	1.410	1.600	1.730	1.840	2.060	2.160	2.280	2.450
NGC 6752	1.360	1.620	1.800	1.950	2.210	2.360	2.520	2.740
NGC 6779	1.249	1.439	1.579	1.689	1.909	1.989	2.079	2.209
NGC 6809	1.752	1.922	2.032	2.132	2.302	2.392	2.492	2.612
NGC 6864	0.710	0.960	1.140	1.300	1.580	1.720	1.880	2.080
NGC 6934	0.959	1.159	1.309	1.439	1.679	1.809	1.959	2.179
NGC 6981	1.169	1.359	1.499	1.609	1.809	1.919	2.049	2.249
NGC 7006	0.839	1.029	1.169	1.289	1.529	1.679	1.879	2.229
NGC 7078	1.048	1.318	1.508	1.658	1.938	2.088	2.258	2.498
NGC 7089	1.178	1.388	1.528	1.658	1.898	2.028	2.178	2.388
NGC 7099	1.070	1.350	1.530	1.670	1.930	2.070	2.240	2.500
NGC 7492	1.418	1.568	1.668	1.758	1.908	1.978	2.058	2.188
PAL 10	1.557	1.807	1.987	2.137	2.397	2.507	2.617	2.727
PAL 11	1.511	1.691	1.801	1.891	2.041	2.121	2.201	2.331
PAL 12	1.278	1.498	1.648	1.768	1.978	2.098	2.248	2.488
PAL 13	0.893	1.043	1.153	1.243	1.393	1.463	1.543	1.633
PAL 1	1.104	1.254	1.394	1.504	1.694	1.774	1.854	1.954
PAL 5	1.771	1.941	2.051	2.141	2.271	2.341	2.421	2.521
PAL 8	1.408	1.628	1.778	1.908	2.128	2.228	2.338	2.438
SMC-KRON 3	1.072	1.262	1.392	1.492	1.692	1.782	1.892	2.042
SMC-NGC 121	0.800	0.990	1.120	1.250	1.520	1.690	1.950	2.370
SMC-NGC 152	1.161	1.361	1.491	1.601	1.801	1.901	2.021	2.201
SMC-NGC 176	0.780	0.970	1.100	1.220	1.480	1.650	1.830	2.010
SMC-NGC 361	1.073	1.263	1.383	1.473	1.633	1.703	1.783	1.883
SMC-NGC 411	0.820	1.020	1.170	1.300	1.540	1.690	1.870	2.140
SMC-NGC 416	0.720	0.910	1.030	1.140	1.340	1.460	1.610	1.810
SMC-NGC 458	0.860	1.060	1.200	1.330	1.570	1.740	1.990	2.430
TERZAN 5	1.099	1.359	1.539	1.699	1.999	2.159	2.349	2.559